ISSN 1674-1056
http://cpb.iphy.ac.cn
http://iopscience.iop.org/cpb
中国物理 B
Chinese Physics
中国物理
Chinese Physics B

Microstructure and magnetocaloric properties in melt-spun and high-pressure hydrogenated $La_{0.5}Pr_{0.5}Fe_{11.4}Si_{1.6}$ ribbons

Qian Liu(刘倩), Min Tong(佟敏), Xin-Guo Zhao(赵新国), Nai-Kun Sun(孙乃坤), Xiao-Fei Xiao(肖小飞), Jie Guo(郭杰), Wei Liu(刘伟), and Zhi-Dong Zhang(张志东)

Citation: Chin. Phys. B, 2021, 30 (**8**): 087502. DOI: 10.1088/1674-1056/abea91
Journal homepage: http://cpb.iphy.ac.cn; http://iopscience.iop.org/cpb

What follows is a list of articles you may be interested in

Some experimental schemes to identify quantum spin liquids

Yonghao Gao(高永豪), Gang Chen(陈钢)
Chin. Phys. B, 2020, 29 (**9**): 097501. DOI: 10.1088/1674-1056/ab9df0

Typicality at quantum-critical points

Lu Liu(刘录), Anders W Sandvik, Wenan Guo(郭文安)
Chin. Phys. B, 2018, 27 (**8**): 087501. DOI: 10.1088/1674-1056/27/8/087501

Entanglement in a two-spin system with long-range interactions

Soltani M R, Mahdavifar S, Mahmoudi M
Chin. Phys. B, 2016, 25 (**8**): 087501. DOI: 10.1088/1674-1056/25/8/087501

Effective model for rare-earth Kitaev materials and its classical Monte Carlo simulation*

Mengjie Sun(孙梦杰)[1,2,†], Huihang Lin(林慧航)[1,†], Zheng Zhang(张政)[1,2], Yanzhen Cai(蔡焱桢)[3], Wei Ren(任玮)[3], Jing Kang(康靖)[3], Jianting Ji(籍建亭)[2], Feng Jin(金峰)[2], Xiaoqun Wang(王孝群)[4,5], Rong Yu(俞榕)[1], Qingming Zhang(张清明)[3,2,‡], and Zhengxin Liu(刘正鑫)[1,§]

[1] *Department of Physics, Renmin University of China, Beijing* 100872, *China*
[2] *Beijing National Laboratory for Condensed Matter Physics, Institute of Physics, Chinese Academy of Sciences, Beijing* 100190, *China*
[3] *School of Physical Science and Technology, Lanzhou University, Lanzhou* 730000, *China*
[4] *Key Laboratory of Artificial Structures and Quantum Control of MOE, Shenyang National Laboratory for Materials Science, Shenyang* 110016, *China*
[5] *School of Physics and Astronomy, Tsung-Dao Lee Institute, Shanghai Jiao Tong University, Shanghai* 200240, *China*

(Received 23 April 2021; revised manuscript received 7 June 2021; accepted manuscript online 11 June 2021)

Recently, the family of rare-earth chalcohalides were proposed as candidate compounds to realize the Kitaev spin liquid (KSL) [*Chin. Phys. Lett.* **38** 047502 (2021)]. In the present work, we firstly propose an effective spin Hamiltonian consistent with the symmetry group of the crystal structure. Then we apply classical Monte Carlo simulations to preliminarily study the model and establish a phase diagram. When approaching to the low temperature limit, several magnetic long range orders are observed, including the stripe, the zigzag, the antiferromagnetic (AFM), the ferromagnetic (FM), the incommensurate spiral (IS), the multi-$\boldsymbol{Q}$, and the 120° ones. We further calculate the thermodynamic properties of the system, such as the temperature dependence of the magnetic susceptibility and the heat capacity. The ordering transition temperatures reflected in the two quantities agree with each other. For most interaction regions, the system is magnetically more susceptible in the *ab*-plane than in the *c*-direction. The stripe phase is special, where the susceptibility is fairly isotropic in the whole temperature region. These features provide useful information to understand the magnetic properties of related materials.

Keywords: Monte Carlo methods, Kitaev materials, quantum spin liquids, rare-earth ions, DM interaction

PACS: 02.70.Uu, 71.70.Ej, 75.10.Kt **DOI:** 10.1088/1674-1056/ac0a5d

1. Introduction

Quantum spin liquid (QSL) is a phase of matter beyond the Landau paradigm, which exhibits a disordered state even at absolute zero temperature due to strong quantum fluctuations. Long-range quantum entanglement instead of long-range correlations (i.e., long-range magnetic orders) is established in the QSL ground states. The elementary excitations in a gapped QSL obey fractional Abelian statistics, or even non-Abelian statistics.[2] Candidate QSL materials with weak spin–orbit couplings have been found in triangular lattice, Kagome lattice, and three-dimensional hyper-Kagome lattice.[3–9]

The Kitaev spin liquids (KSL), either gapless or gapped, are a special type of QSLs which are exact ground states of a simple honeycomb lattice spin model.[10] A magnetic field can drive the gapless KSL into a non-Abelian chiral QSL which hosts non-Ablian anyons and has potential applications in quantum computations.[11–13] Several materials, including the well studied α-$RuCl_3$, were proposed to realize the Kitaev interactions.[14–30] The Ru^{3+} ions behave like spin-1/2 spins whose exchange interactions contain the Kitaev terms.[29,31–35] However, the ground state falls outside the KSL phase since the material exhibits zigzag-type long-range magnetic order at low temperatures.[14–18,22] This indicates that additional non-Kitaev (K) interactions exist, such as Heisenberg (J) terms and off-diagonal symmetric interactions (such as Γ and Γ' terms).[23,29,31,36,37]

Besides the transition metal compounds, the rare-earth chalcogenide families are also QSL candidates. The rare-earth chalcogenide materials $A\mathrm{RECh}_2$ (where A = alkali or monovalent ions, RE = rare-earth, Ch = O, S, Se) on triangular lattice, such as $NaYbO_2$, have attracted much attention.[38–40] On the other hand, the family of honeycomb lattice rare-earth chalcohalides REChX (RE = rare earth, Ch = O, S, Se,Te, X = F, Cl, Br, I), such as YbOCl and SmSI, provides alternative possibilities to realize Kitaev QSLs.[1] The REChX family is a good quasi-two-dimensional material due to the lager

*Project supported by the National Key Research and Development Program of China (Grant Nos. 2017YFA0302904 and 2016YFA0300504), the National Natural Science Foundation of China (Grant Nos. U1932215, 11774419, 11574392, and 11974421), the Strategic Priority Research Program of the Chinese Academy of Sciences (Grant No. XDB33010100), the Fundamental Research Funds for the Central Universities, China, and the Research Funds of Renmin University of China (Grant No. 19XNLG11). Q. M. Z. acknowledges the support from Users with Excellence Program of Hefei Science Center and High Magnetic Field Facility, CAS.

†These authors contributed to the work equally.
‡Corresponding author. E-mail: qmzhang@ruc.edu.cn
§Corresponding author. E-mail: liuzxphys@ruc.edu.cn

© 2021 Chinese Physical Society and IOP Publishing Ltd

distance between layers. Furthermore, the strong crystalline electronic field (CEF) owing to chalcogen ion ensures that the effective spin of the rare earth ion is spin-1/2. The strong spin–orbital coupling results in anisotropic exchange interactions. The physical properties of YbOCl in the temperature range of 1.8 K–300 K have been reported in Ref. [1], but the microscopic effective model needs to be investigated.

In this work, we first discuss possible interactions in YbOCl based on symmetry analysis. The potential Hamiltonian includes the Heisenberg terms (J), the Kitaev terms (K), the off diagonal terms (Γ, Γ'), and the DM interactions. We then study the resultant model Hamiltonian using classical Monte Carlo simulation, and obtain the preliminary phase diagram, which includes the stripe phase, the zigzag phase, the antiferromagnetic (AFM) phase, the ferromagnetic (FM) phase, the 120° phase, the incommensurate spiral (IS) phase, and the multi-$\boldsymbol{Q}$ phase. We further calculate thermodynamic properties such as the temperature dependence of the magnetic susceptibility and the heat capacity, which may help to determine the interaction parameters and to understand the magnetic and thermal properties at low temperatures in real materials.

2. Symmetry allowed spin–spin interactions

2.1. Structure and symmetry

The layered rare-earth material YbOCl belongs to the SmSI family with ABCABC stacking structure, and its space group symmetry is 166 ($R\bar{3}m$),[1,41] as illustrated in Fig. 1(a). The Yb^{3+} ions form two adjacent layers of triangular lattice, whose lattice constant in each layer reads $d_2 = 3.72$ Å. The two layers nest with each other to form a rough 'honeycomb lattice', where the distance between nearest neighbors (the nearest bond linking the two triangular layers) is $d_1 = 3.545$ Å, which is smaller than d_2. Although the two layers of triangular lattice do not have C_6 rotation or σ_h mirror reflection symmetry, the combined operation $S_6 = C_6\sigma_h$ is indeed a symmetry element (here the mirror plane σ_h locates at the middle of the two triangular layers). Moreover, the distance between two adjacent honeycomb layers is $d_3 = 6.443$ Å, which is much larger than d_2. Therefore, we can treat YbOCl as a quasi-two-dimensional material with honeycomb lattice structure.

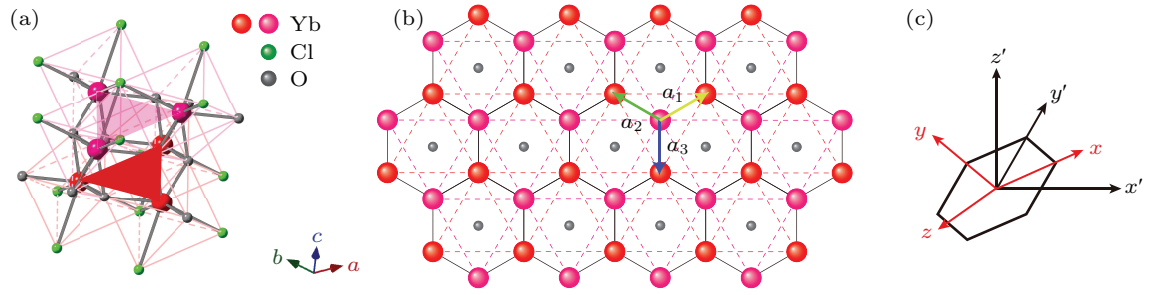


Fig. 1. (a) The crystal structure of YbOCl. (b) The quasi honeycomb lattice 'plane' (called the ab-plane with the normal direction c) formed by the Yb^{3+}. (c) The conventional frame ($\hat{x}'$, $\hat{y}'$, $\hat{z}'$) vs. the new frame ($\hat{x}$, $\hat{y}$, $\hat{z}$), where $\hat{x}' = \frac{1}{\sqrt{2}}(\hat{x}-\hat{y})$, $\hat{y}' = \frac{1}{\sqrt{6}}(\hat{x}+\hat{y}-2\hat{z})$, $\hat{z}' = \frac{1}{\sqrt{3}}(\hat{x}+\hat{y}+\hat{z})$.

Each Yb^{3+} ion is surrounded by three Cl^- (the angle formed by the bonds Cl–Yb–Cl is 85.505°) and four O^{2-} (the angle formed by the bonds O–Yb–O is 76.229° or 114.52°). These anions form the complex polyhedral CEF environment for the magnetic ion Yb^{3+} with site group $\mathscr{C}_{3v}$. The electronegativity of coordination anion Cl^- and O^{2-} is very strong, and the energy splitting caused by the CEF is of order of 65 meV, which is much larger than the band width ($\sim$ 10 meV) of the low-lying energy level. Therefore, the system maintains an effective spin $S = 1/2$ local moment at a large temperature range. The nearest neighbor sites perform super-exchange interaction through O^{2-}, while the next nearest-neighbor sites perform it through both Cl^- and O^{2-}. Since the orbits of the Yb^{3+} ions are fairly local, the intensity of the super-exchange interaction is relatively weak which is of order of 1 K.[39,42–48]

Since the $R\bar{3}m$ group is symmorphic, its point group D_{3d} precisely describes the symmetry of the center of the unit cell. The D_{3d} point group is generated by S_6 and C_2, where the S_6 symmetry operation was illustrated previously. The two-fold rotation axis C_2 lies in the mirror plane of S_6 and points from the center of the unit cell to the bond center of two adjacent Yb^{3+} ions (this C_2 axis is perpendicular to the bond direction, in contrast to the standard orientation of the Kitaev model where the C_2 axis is along the bond direction[49,50]). The D_{3d} point group determines the possible effective interactions between the Yb^{3+} spins.

The 4f electrons in Yb^{3+} ions have a strong spin–orbit coupling (of order of 0.36 eV). This indicates that the effective interactions have a strong anisotropy. Actually, the strong electronegativity of O^{2-} makes the bonds strongly ionic, which causes a higher tendency of performing super-exchange interactions between cations and coordination anions. Meanwhile, adjacent polyhedrons share the same side, thus the Heisenberg interactions are suppressed and the rest interactions are strongly anisotropic.[32]

Recall that the Kitaev honeycomb lattice model also has a D_{3d} point group symmetry when considering spin–orbit coupling, which is the same as the point group of YbOCl. There-

fore it is natural to infer that the low-energy effective model of YbOCl contains the Kitaev type interactions (the K terms). This makes YbOCl a possible Kitaev material. Like most Kitaev materials, the Kitaev interaction has negative sign($K<0$). Other interactions are also allowed as long as they are consistent with the D_{3d} symmetry. We will discuss the effective spin–spin interactions in Subsection 2.2.

2.2. Low-energy effective Hamiltonian model

As mentioned above, the symmetry group D_{3d} of YbOCl is consistent with that of the Kitaev model. In the Kitaev model, owing to spin–orbit coupling, the c-axis is parallel to the $\frac{1}{\sqrt{3}}(\hat{x}+\hat{y}+\hat{z})$ direction in the spin frame such that a C_3 rotation permutes $\hat{x}$, $\hat{y}$, $\hat{z}$ cyclically. Here we adopt the same convention. Furthermore, the horizontal direction (i.e., the C_2 axis) is identified as $\frac{1}{\sqrt{2}}(\hat{x}-\hat{y})$, and the vertical direction is indentified as $\frac{1}{\sqrt{6}}(\hat{x}+\hat{y}-2\hat{z})$. Hence we obtain the most general Hamiltonian of the family of rare-earth chalcohalides:[39,42–47,51–56]

$$\begin{aligned} H = & \sum_{\langle i,j\rangle\in\alpha\beta(\gamma)} KS_i^\gamma S_j^\gamma + J\boldsymbol{S}_i\cdot\boldsymbol{S}_j + \Gamma(S_i^\alpha S_j^\beta + S_i^\beta S_j^\alpha) \\ & + \Gamma'(S_i^\alpha S_j^\gamma + S_i^\gamma S_j^\alpha + S_i^\beta S_j^\gamma + S_i^\gamma S_j^\beta) \\ & + \sum_{\langle\langle ij\rangle\rangle} \boldsymbol{D}_{ij}\cdot(\boldsymbol{S}_i\times\boldsymbol{S}_j), \end{aligned} \tag{1}$$

where α,β,γ label the type of the nearest neighbor bonds and the spin indices, and $\langle i,j\rangle$, $\langle\langle i,j\rangle\rangle$ denote the nearest-neighbor and the next nearest-neighbor sites, respectively.

The last term in Eq. (1) is the DM interaction on the next nearest-neighbor bonds, which is assumed to be stronger than other interactions on the same bonds. Structurally, the $\boldsymbol{D}_{ij}$ vector takes the following form $\boldsymbol{D}_{ij}=D(\boldsymbol{r}_i\times\boldsymbol{r}_j)$ with $\boldsymbol{r}_i$ the position vector pointing from the ith magnetic ion to the coordination anion which mediates the super-exchange. For YbOCl, the next nearest-neighbor rare-earth ions mainly exchange through the O^{2-} ions (the other type anions Cl^- are far away from the next-nearest bonds and have weaker effects). Since the O^{2-} anions are almost locating in the cation layer, it is expected that the DM vector $\boldsymbol{D}_{ij}$ is almost pointing along the c-direction (namely, the [1,1,1] direction in the spin frame).

Here we clarify the difference between the conventional spin frame (we label the axes as $\hat{x}'$, $\hat{y}'$, $\hat{z}'$) and the one introduced above. Since the D_{3d} point group has only one high-symmetry axis $\hat{c}$, conventionally the $\hat{c}$ axis is chosen to be the $\hat{z}'$-axis, the horizontal line is identified with the $\hat{x}'$-axis, and the vertical line is identified with the $\hat{y}'$-axis (see Fig. 1 for illustration). In other words, in the conventional spin frame, the axes are parallel to the corresponding ones of the lattice frame. The spin operators in the two frames are related in the following way:

$$S'^x=\frac{1}{\sqrt{2}}(S^x-S^y),$$

$$S'^y=\frac{1}{\sqrt{6}}(S^x+S^y-2S^z),$$

$$S'^z=\frac{1}{\sqrt{3}}(S^x+S^y+S^z).$$

The symmetry operations act differently in the two frames. Owing to the spin–orbital coupling, the point group symmetry elements not only transform the sites but also transform the spins in the same way. For instance, if i and j label two sites on a nearest neighbor z-bond, then in the symmetric spin frame, S_6 transforms $S_i^{x,y,z}$ to $S_j^{z,x,y}$, and C_2 operation transforms $S_i^{x,y,z}$ to $-S_j^y,-S_j^x,-S_j^z$, respectively. However, in the conventional frame, S_6 transforms $S_i'^x,S_i'^y,S_i'^z$ to

$$S_6S_i'^xS_6^{-1}=-\frac{1}{2}S_j'^x-\frac{\sqrt{3}}{2}S_j'^y,$$

$$S_6S_i'^yS_6^{-1}=\frac{\sqrt{3}}{2}S_j'^x-\frac{1}{2}S_j'^y,$$

$$S_6S_i'^zS_6^{-1}=S_j'^z,$$

respectively, and C_2 transforms $S_i'^x,S_i'^y,S_i'^z$ to

$$C_2S_i'^xC_2^{-1}=S_j'^x,\quad C_2S_i'^yC_2^{-1}=-S_j'^y,\quad C_2S_i'^zC_2^{-1}=-S_j'^z,$$

respectively.

In the conventional spin frame, the model (1) takes a different form (see Appendix A). Under the above rule of symmetry transformations, the transformed model still preserves the D_{3d} symmetry group.

3. Preliminary results of the model

3.1. Classical Monte Carlo simulation

We use the classical Monte Carlo (MC) method to numerically simulate the model (1), where the spins are treated as classical three-component unit vectors. Since Γ' is generally small in Kitaev materials,[57,58] we set $\Gamma'=0$ in our calculations. We firstly investigate the case with $\boldsymbol{D}_{ij}=0$, and then study the effect of the DM interactions. We aim to determine the phase diagram of the classical ground states, and provide the critical temperatures of each ordered phase.

In our classical MC simulation, the spin configurations are distributed with a probability proportional to $\exp\{-\frac{E}{k_BT}\}$ (where E is the total energy of the system) according to Boltzmann statistics. Metropolis algorithm is applied to update the spin configurations in the MC sampling.

However, for the honeycomb lattice model the slowing down of configuration updating is very serious when approaching the critical temperatures. To solve this problem, we use the microcanonical over-relax algorithm to reduce the autocorrelation time and replace the usual MC steps by the 'mixed' MC steps. Generally, the over-relax algorithm makes the spin rotate at any angle around the local equivalent field,[59] so that the total energy will not be changed. The simplest and most effective method is to make the spin rotate π

angle around the local equivalent field, which is actually adopt in our MC simulations. There is no need to generate random numbers to achieve such spin flip, thus saving the simulation time. Practically we extend each usual MC step (a usual MC step consists of N times of trial spin flip) by a mixed MC step, which consists of a usual MC step and some over-relaxation updates. The deterministic change of spin is very important to reduce the autocorrelation time at low temperatures. According to the lattice size, we increase the number of over-relaxation updates per MC step.

Finally, to avoid being trapped into local minima, we apply the annealing algorithm in the low temperature region.

In our simulation, the system size is $N = 2 \times L^2$, with $L = 24$. Periodic boundary condition is adopt. For each parameter point, the system is preheated by 5×10^5 times to reach the thermal equilibrium, then measurements are made every three MC steps. The total number of measurements is 5×10^5.

3.2. The phase diagram

Figure 2 shows the magnetic phase diagram of the classical ground states with $\Gamma' = 0$, $\boldsymbol{D}_{ij} = 0$ (the model with the same parameters was studied using different methods[31,37,60–66]). Five phases are obtained, namely, the stripe, the antiferromagnetic (AFM), the ferromagnetic (FM), the incommensurate spiral (IS), and the zigzag phases. Except for the IS phase, all the other magnetic orders are collinear. To identify the magnetic phases, we plot the spin configurations in real space, as shown in Figs. 2(d)–2(g). The orientation of the magnetic momentums in each phase is the following: the stripe phase $\boldsymbol{M}_i \parallel [1,0,0]$ (equivalent orientations related by the symmetry group also include $[0,1,0]$ and $[0,0,1]$, here and later we only list one of them), the AFM phase $\boldsymbol{M}_i \parallel [1,1,1]$, the FM phase $\boldsymbol{M}_i$ approximately parallel to $[5,3,-8]$, and the zigzag phase $\boldsymbol{M}_i \parallel [1,-1,1]$.

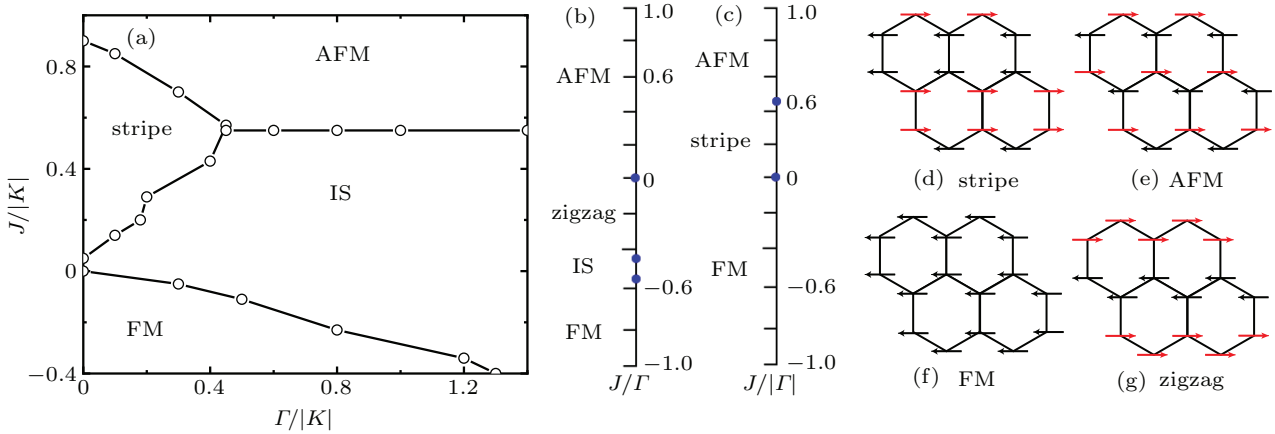


Fig. 2. (a) Phase diagram of the classical J–K–Γ ($K < 0$) model, which contains the stripe, the antiferromagnetic (AFM), the ferromagnetic (FM), and the incommensurate spiral (IS) phases. (b) Phase diagram of the classical J–Γ model for $\Gamma > 0$; the transitions occur at $J/\Gamma = 0$, -0.45, and -0.55. (c) Phase diagram of the classical J–Γ model for $\Gamma < 0$; the transitions occur at $J/|\Gamma| = 0$ and 0.45. (d)–(g) The spin configurations in different magnetic orders. Except for the IS phase, all the other magnetic orders are collinear. The orientation of the magnetic momentums in each phase is the following: the stripe $\boldsymbol{M}_i \parallel [1,0,0]$, the AFM $\boldsymbol{M}_i \parallel [1,1,1]$, the FM $\boldsymbol{M}_i \parallel [5,3,-8]$, and the zigzag $\boldsymbol{M}_i \parallel [1,-1,1]$.

We also calculate the static spin structure factor. Each phase is characterized by the Bragg peaks in the reciprocal lattice, as shown in Fig. 3. The stripe phase and zigzag phase are both peaked at three C_3 symmetry-related M points, namely, the midpoint of the hexagonal edge of the Brillouin zone. Since the two types of orders have the same inter unit-cell patterns but different intra unit-cell patterns, the positions of the Bragg peaks in the two phases differ by a reciprocal lattice vector. Similarly, the FM phase has a Bragg peak at the center of the BZ, while the AFM phase is peaked at the boundary of the BZ. The static structure factor of the IS phase is peaked at several equivalent non-high-symmetry points which are related by symmetry.

The magnetic ground state of the system is the stripe phase when $0 < J/|K| < 0.9$ and is the AFM phase when $J/|K| > 0.9$, where J is the antiferromagnetic interaction and $\Gamma = 0$. When the strengths of J and K are basically the same, the Heisenberg (J) interaction dominates and the system enters the AFM phase. When both J and K are ferromagnetic, the ground state of the system naturally enters the FM phase. Next, we focus on the regulation of Γ in the pure J–K model. Antiferromagnetic Γ will cause transition from the stripe phase to the AFM phase or the IS phase. And Γ will also cause transition from the FM phase to the IS phase. Experimentally, most of the Kitaev materials fall in the zigzag phase or the IS phase, indicating the existence of Γ and other interactions.

In order to analyze the regulation of Γ on J interaction, we simulate the ground state magnetic phase diagram of $J/|\Gamma|$ when $K = 0$, as shown in Figs. 2(b) and 2(c). Γ in Fig. 2(b) is the antiferromagnetic exchange interaction. When $J/\Gamma > 0$, the ground state of the system is the AFM phase. When $J = 0$, the system enters the multi-$\boldsymbol{Q}$ state. When $-0.45 < J/\Gamma < 0$, the system transits to the zigzag phase, namely, the system

can also enter the zigzag phase when only J and Γ interactions exist. When $-0.55 < J/\Gamma < -0.45$, the system enters the IS phase again. It can be seen that the zigzag phase and the IS phase are always related to each other, indicating that they may have similar energy. When $J/\Gamma < -0.55$, the system enters the conventional FM phase.

Figure 2(c) is the the phase diagram with $\Gamma < 0$, $K = 0$. When J is antiferromagnetic interaction and $J/|\Gamma| > 0.45$, the ground state of the system is the AFM phase, which is natural under large antiferromagnetic Heisenberg interaction. But when $0 < J/|\Gamma| < 0.45$, the system enters the stripe phase. When $J = 0$, the system also enters the multi-$\boldsymbol{Q}$ state. And when $J/|\Gamma| < 0$, the system no longer enters the strange magnetic ordered phase, but directly enters the FM phase.

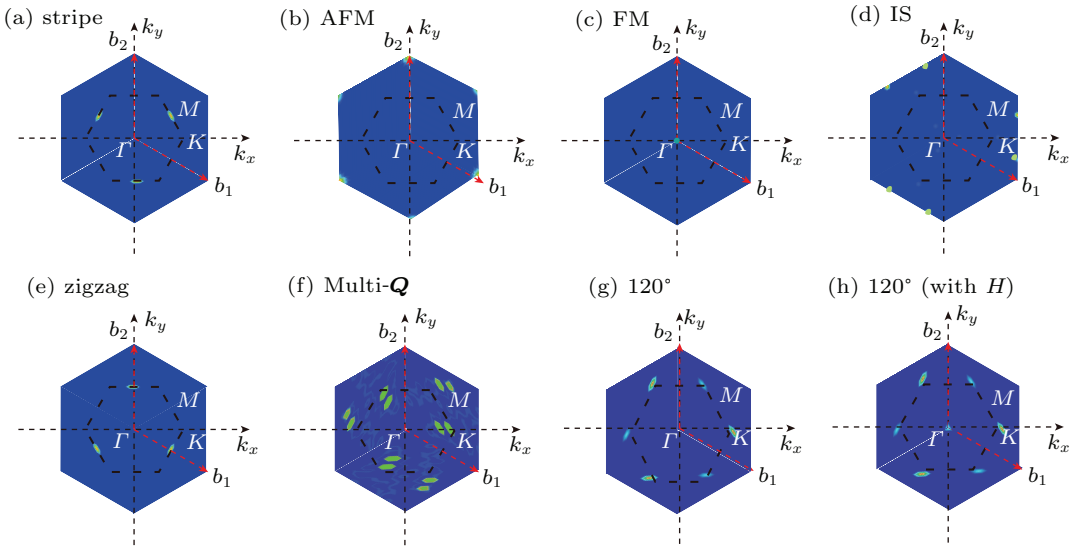


Fig. 3. Low-T MC static structure factor for J–K–Γ–$\boldsymbol{D}$ ($K < 0$) model. Bright spots indicate Bragg peaks. The dotted inner hexagon denotes the first Brillouin zone. (a)–(h) The static structure factors of the stripe, the AFM, the FM, the IS, the zigzag, the multi-$\boldsymbol{Q}$, the 120° order, and the 120° order in magnetic field.

3.3. The thermodynamic quantities

In order to study the magnetic properties of each magnetic ordered phase, we simulate the thermodynamic quantities, including the susceptibility and the heat capacity, for each phase in the phase diagram.

From the fluctuation–dissipation theorem, the above thermal quantities can be evaluated in the MC simulations from the correlation functions of the corresponding physical quantities, namely,

$$C(T) = (\langle E^2\rangle - \langle E\rangle^2)/(NT^2),$$
$$\chi_\alpha(T) = (\langle M_\alpha^2\rangle - \langle M_\alpha\rangle^2)/(NT).$$

The susceptibility, as a tensor, has the same point group symmetry as the crystal, which is D_{3d}. Since the material is uni-axial, so the magnetic susceptibility has two different eigenvalues χ_c and χ_{ab} (the symmetry guarantees that the magnetic susceptibility in the ab-plane is isotropic). In all of the magnetic phases, χ_c is smaller than χ_{ab}, meaning that the spins are more susceptible along the ab-plane and the c-direction is a hard axis. At high temperature region, the susceptibility obeys the Curie law. In order to accurately identify the phase transition temperatures, the quantity $\mathrm{d}(\chi T)/\mathrm{d}T$ is also plotted, whose singular points indicate the transitions.

For most of the ordered phases, the susceptibility shows a λ-shape peak near the critical point in two directions. However, for the zigzag phase there is no obvious peak in χ_c near the phase transition point. Instead, a plateau appears near the phase transition point and then monotonously increases with decreasing temperature. χ_{ab} has obvious λ-shape peak, and the phase transition occurs at the point where the susceptibility decreases most rapidly.

The χ_{ab} of IS is also very unusual, which shows a strange double-peak structure, the one at the low-temperature side is sharp and the other is relatively boarder. The structure factor and susceptibility demonstrate that the sharp peak represents the phase transition. Therefore, the phase transition temperature of IS order is very low, indicating that the system remains fluctuating and forms the IS order only at very low temperatures.

The magnetic susceptibility in the stripe phase is almost isotropy. The AFM order is arranged in the [1,1,1] direction, so χ_c approaches zero but χ_{ab} remains finite at zero temperature.

The transition temperatures identified from the heat capacity (see Fig. 5) are basically consistent with those obtained from the $\mathrm{d}(\chi T)/\mathrm{d}T$. The heat capacity shows a sharp peak in the transition point to the stripe phase, or the AFM phase, or the FM phase. The zigzag and IS phase are special, since there is a shoulder like structure in the heat capacity at the right hand side of the transition point.

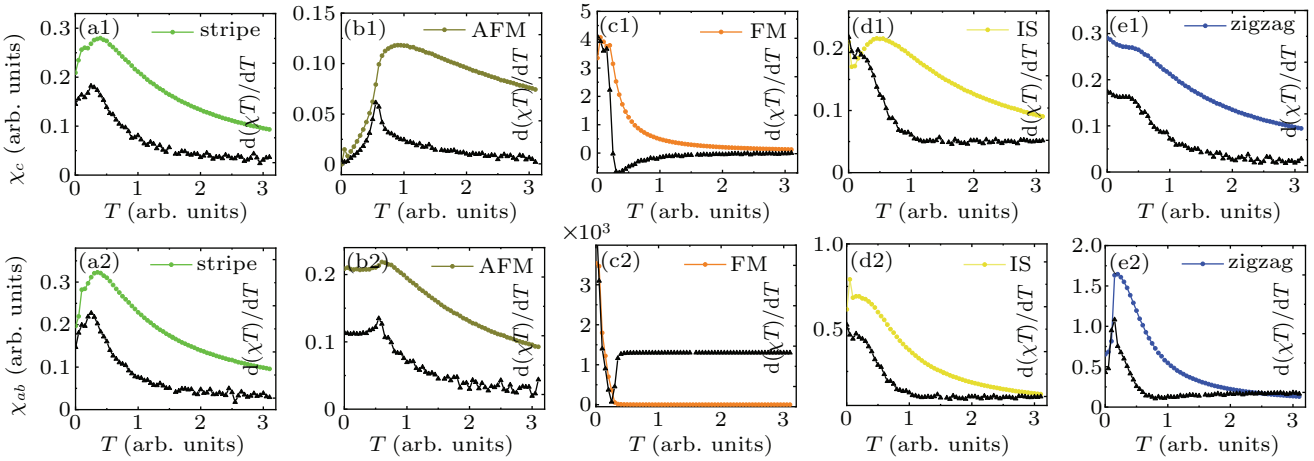


Fig. 4. The susceptibility χ_c and χ_{ab} for different magnetic ordered phases: (a) the stripe with $\Gamma/|K| = 0.1$, $J/|K| = 0.5$, (b) the AFM with $\Gamma/|K| = 0.8$, $J/|K| = 1$, (c) the FM with $\Gamma/|K| = 0.4$, $J/|K| = -0.35$, (d) the IS with $\Gamma/|K| = 0.8$, $J/|K| = 0.3$, (e) the zigzag with $J/\Gamma = -0.2$ ($K = 0$). The colored curves show the susceptibility χ, the dark ones illustrate $\mathrm{d}(\chi T)/\mathrm{d}T$ (the data have been multiplied by some constant to guide the eyes) from which the transition points can be easily read out.

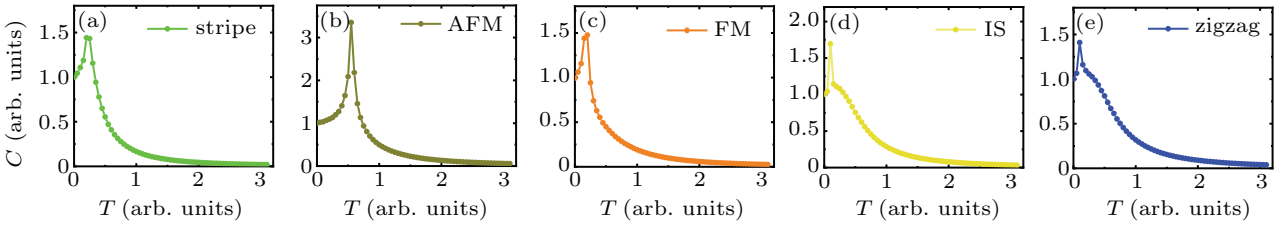


Fig. 5. The heat capacity of different magnetically ordered phases and their corresponding high temperature paramagnetic phases. The interaction parameters of (a)–(e) are the same as the corresponding ones provided in the caption of Fig. 4.

These features of the magnetic susceptibility in Fig. 4 and the specific heat in Fig. 5 are helpful to identity the magnetic orders in real materials.

However, it should be realized that in the low temperature limit, quantum effects can not be neglected even in the ordered phases. In the pure classical model, since the energy is a continuous function of spin configurations, the specific heat has a finite residue value at zero temperature (it is of order 1 in all of the magnetic phases, see Fig. 5). By considering the quantum corrections in the semi-classical linear spin wave theory, the residue specific heat should be zero. If the magnon excitations are gapless, then the specific heat should decay to zero in power law when T approaches to zero, namely, $C(T) \propto T^n$ (where n is an integer); otherwise, if the magnons are gaped, then $C(T)$ decays exponentially with lowering temperature, namely, $C(T) \propto \mathrm{e}^{-\Delta/k_\mathrm{B}T}$ with Δ being the magnon gap and k_B the Boltzmann constant. In both cases, $C = 0$ at $T = 0$, which is consistent with the zeroth law of thermodynamics. Similarly, the low-temperature behavior of the magnetic susceptibility in Fig. 4 should also be strongly affected by quantum fluctuations.

3.4. Effect of the DM interaction

In this subsection we study the effect of the next nearest-neighbor DM interaction with $\boldsymbol{D} \parallel [1,1,1]$. A finite $|D|$ dramatically changes the phase diagram. For instance, at fixed $|D|/|K| = 0.2$, the magnetic phase diagram of the classical ground states is shown in Fig. 6(a).

Compared to Fig. 2(a), the main difference is that the IS phase is replaced by two new phases (a shortened IS phase should remains if $|D|$ is smaller), the 120° phase and the multi-$\boldsymbol{Q}$ phase. The static structure factor of the 120° phase is peaked at K points while the static structure factor of the multi-$\boldsymbol{Q}$ phase is peaked at more than one non-equivalent momentum points, see Figs. 3(g) and 3(f), respectively.

The 120° phase occurs at the region $0 < J < 0.6$ and $\Gamma/|K| < 0.94$. The multi-$\boldsymbol{Q}$ phase roughly locates at $-0.2 < J < 0$ as $\Gamma/|K| < 0.6$. When $\Gamma/|K| > 0.6$, the multi-$\boldsymbol{Q}$ phase competes with the 120° phase and completely beats it as $\Gamma/|K| > 0.94$. Furthermore, the sizes for all of the rest phases are shortened. The lower boundary of the AFM phase slightly goes up, and the upper boundary of the FM phase moves down. The stripe phase as a whole slightly moves up, giving part of its place to the 120° phase.

From the above analysis, we can see the strong preference of the 120° phase and the multi-$\boldsymbol{Q}$ phase by the out-of-plane DM interactions. In order to explore the critical DM interaction, we simulate the magnetic phase transitions with increasing $|D|/|K|$ in different magnetic phase regions, as shown in Figs. 6(b)–6(d).

At $\Gamma/|K| = 0.1$, $J/|K| = 0.3$, the stripe phase turns to the 120° phase at $|D|/|K| = 0.1$.

At $\Gamma/|K| = 0.5$, $J/|K| = 0.2$, the IS (J is antiferromagnetic interaction) phase is replaced by the multi-$\boldsymbol{Q}$ phase at an extremely small DM interaction, and then transits to the 120° phase at $|D|/|K| = 0.1$.

At $\Gamma/|K| = 0.8$, $J/|K| = -0.1$, the IS phase survives for a finite region of D, until it is replaced by the multi-$\boldsymbol{Q}$ phase as $|D|/|K| > 0.2$.

Finally, we preliminarily study the effect of magnetic field in the presence of DM interactions. Figure 6(e) shows the phase diagram of the $\Gamma/|K|$ with $\boldsymbol{H} \parallel [1,1,1]$, $J/|K| = 0.4$, and $|D|/|K| = 0.2$. The 120° phase is robust against magnetic field with its static structure factor peaks at both the K points and the center of the BZ [see Fig. 3(e) for illustration]. The inset illustrates the in-plane ordering pattern (the out-of-plane components which are partially polarized by the field are not shown). Firstly, when the field is weaker than $g\mu_B H/|K|$, the multi-$\boldsymbol{Q}$ phase is suppressed and the 120° phase is enlarged. Secondly, when the filed is strong enough, the 120° order will be destroyed at a critical field strength. It turns out that the critical field strength increases with the increase of $\Gamma/|K|$.

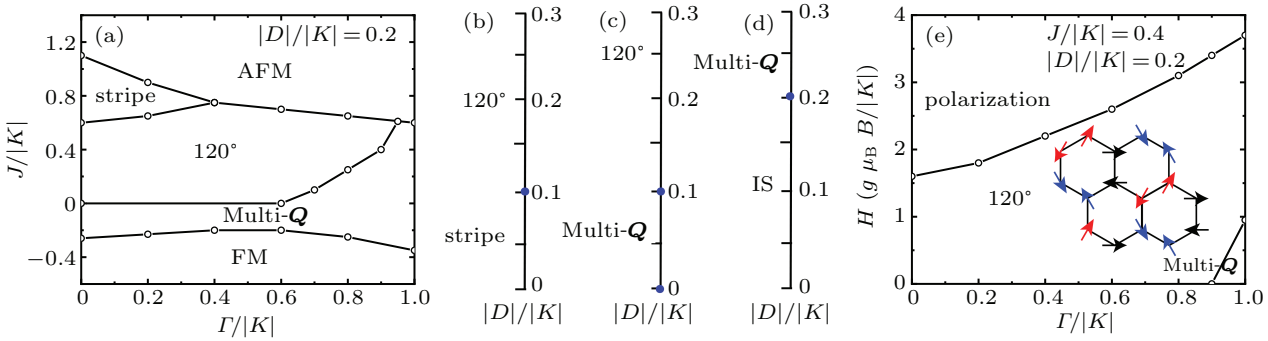


Fig. 6. (a) Phase diagram of the classical J–K–Γ ($K < 0$, $|D|/|K| = 0.2$) model, which contains the stripe, the antiferromagnetic (AFM), the ferromagnetic (FM), the 120° order, and the multi-$\boldsymbol{Q}$ phases. (b) For $J/|K| = 0.3$, $\Gamma/|K| = 0.1$, the transitions occur at $|D|/|K| = 0.1$. (c) For $J/|K| = 0.2$, $\Gamma/|K| = 0.5$, the transitions occur at $|D|/|K| = 0$ and 0.1. (d) For $J/|K| = -0.1$, $\Gamma/|K| = 0.8$, the transitions occur at $|D|/|K|$=0.2. (e) Phase diagram of the $\Gamma/|K|$ with $\boldsymbol{H} \parallel [1,1,1]$ ($J/|K| = 0.4$ and $|D|/|K| = 0.2$); the inset illustrates the in-plane spin configurations in the 120° ordered phase.

When quantum effects are taken into account, an out-of-plane DM interaction and a magnetic field can cause thermal Hall effect since the magnon excitations (in the ordered phase) or the spinon excitations (in the disordered phase) will feel nonzero Berry phase.[67,68] Furthermore, in-plane DM interactions and out-of-plane magnetic field may generate skyrmion excitations at suitable temperature region.[69] These possibilities make the rare-earth chalcohalide a platform to explore the interesting physics.

4. Discussion and conclusion

In summary, we have studied the magnetism of rare-earth chalcohalides as candidate materials of Kitaev QSL. Based on the crystal structure and symmetry group, a low-energy effective model is proposed. We calculate the classical phase diagram of the magnetic ground state of the J–K–Γ–$\boldsymbol{D}$ model using classical Monte Carlo method. We identify the classical magnetic orders in the ground states, including the stripe, the zigzag, the antiferromagnetic (AFM), the ferromagnetic (FM), the incommensurate spiral (IS), the multi-$\boldsymbol{Q}$, and the 120° order. The next nearest-neighbor DM interaction strongly prefers the 120° and the multi-$\boldsymbol{Q}$ phase. The temperature dependence of the magnetic susceptibility and the heat capacity are provided, which may help to experimentally identify the magnetic orders and to understand their low-temperature behaviors.

The family of rare-earth chalcohalides provides an ideal platform for the further study of Kitaev QSLs. The parameters of the effective model for the YbOCl and other materials in the family need to be determined from further experimental measurements (such as inelastic neutron scattering). On the other hand, the quantum phase diagram of the model with nonzero next-nearest neighbor interactions (DM and other possible interactions) needs to be figure out using quantum many-body computation methods. We leave these studies to future work.

Appendix A: Hamiltonian transformation in different coordinate systems

Notice that the D_{3d} point group has only one high-symmetry axis. Usually this axis is chosen to be the $\hat{z}'$-axis for both the lattice frame and the spin frame. The Hamiltonian will be complicated when the spin and lattice share the same conventional frame $\{x', y', z'\}$ (see Fig. 1(c)). And the D_{3d} symmetry can be expressed by introducing a higher symmetric frame for the spin axis. The spin coordinate system is changed to $\{x, y, z\}$ (see Fig. 1(c)) after corresponding rotation. In the new coordinate system, $\{x', y', z'\}$ unit vector can be expressed as $\hat{x}' = \frac{1}{\sqrt{2}}(1,-1,0)$, $\hat{y}' = \frac{1}{\sqrt{6}}(1,1,-2)$, $\hat{z}' = \frac{1}{\sqrt{3}}(1,1,1)$.

In other words, the spin components in Hamiltonian (1) can be expressed as

$$S^x = \frac{\sqrt{2}}{2}S'^x + \frac{\sqrt{6}}{6}S'^y + \frac{\sqrt{3}}{3}S'^z,$$

$$S^y = \frac{-\sqrt{2}}{2}S'^x + \frac{\sqrt{6}}{6}S'^y + \frac{\sqrt{3}}{3}S'^z,$$
$$S^z = \frac{-\sqrt{6}}{3}S'^y + \frac{\sqrt{3}}{3}S'^z.$$

By introducing the transformed spin into Hamiltonian (1), we can get the spin Hamiltonian model in conventional frame $\{x', y', z'\}$

$$\begin{aligned}
H_x = & \sum_{\langle i,j=i+a_1\rangle}\left(J+\frac{K}{2}-\Gamma'\right)S'^x_i S'^x_j \\
&+\left(J+\frac{K}{6}-\frac{2}{3}\Gamma-\frac{1}{3}\Gamma'\right)S'^y_i S'^y_j \\
&+\left(J+\frac{K}{3}+\frac{2}{3}\Gamma+\frac{4}{3}\Gamma'\right)S'^z_i S'^z_j \\
&+\left(\frac{\sqrt{3}}{6}K+\frac{\sqrt{3}}{3}\Gamma-\frac{\sqrt{3}}{3}\Gamma'\right)(S'^x_i S'^y_j+S'^y_i S'^x_j) \\
&+\left(\frac{\sqrt{6}}{6}K-\frac{\sqrt{6}}{6}\Gamma+\frac{\sqrt{6}}{6}\Gamma'\right)(S'^x_i S'^z_j+S'^z_i S'^x_j) \\
&+\left(\frac{\sqrt{2}}{6}K-\frac{\sqrt{2}}{6}\Gamma+\frac{\sqrt{2}}{6}\Gamma'\right)(S'^y_i S'^z_j+S'^z_i S'^y_j), \\
H_y = & \sum_{\langle i,j=i+a_2\rangle}\left(J+\frac{K}{2}-\Gamma'\right)S'^x_i S'^x_j \\
&+\left(J+\frac{K}{6}-\frac{2}{3}\Gamma-\frac{1}{3}\Gamma'\right)S'^y_i S'^y_j \\
&+\left(J+\frac{K}{3}+\frac{2}{3}\Gamma+\frac{4}{3}\Gamma'\right)S'^z_i S'^z_j \\
&+\left(-\frac{\sqrt{3}}{6}K-\frac{\sqrt{3}}{3}\Gamma+\frac{\sqrt{3}}{3}\Gamma'\right)(S'^x_i S'^y_j+S'^y_i S'^x_j) \\
&+\left(-\frac{\sqrt{6}}{6}K+\frac{\sqrt{6}}{6}\Gamma-\frac{\sqrt{6}}{6}\Gamma'\right)(S'^x_i S'^z_j+S'^z_i S'^x_j) \\
&+\left(\frac{\sqrt{2}}{6}K-\frac{\sqrt{2}}{6}\Gamma-\frac{\sqrt{2}}{6}\Gamma'\right)(S'^y_i S'^z_j+S'^z_i S'^y_j), \\
H_z = & \sum_{\langle i,j=i+a_3\rangle}(J-\Gamma)S'^x_i S'^x_j \\
&+\left(J+\frac{2}{3}K+\frac{1}{3}\Gamma-\frac{4}{3}\Gamma'\right)S'^y_i S'^y_j \\
&+\left(J+\frac{K}{3}+\frac{2}{3}\Gamma+\frac{4}{3}\Gamma'\right)S'^z_i S'^z_j \\
&+\left(-\frac{\sqrt{2}}{3}K+\frac{\sqrt{2}}{3}\Gamma-\frac{\sqrt{2}}{3}\Gamma'\right)(S'^y_i S'^z_j+S'^z_i S'^y_j),
\end{aligned}$$

where H_x, H_y, H_z is the Hamiltonian of the x-, y-, z-bond, respectively. Above Hamiltonian can take a compact form by a 90° rotation, $\hat{x}' \to \hat{y}' = \frac{1}{\sqrt{6}}(1,1,-2)$, $\hat{y}' \to -\hat{x}' = \frac{1}{\sqrt{2}}(-1,1,0)$, $\hat{z}' = \frac{1}{\sqrt{3}}(1,1,1)$. Thus the effective model is transformed into[51]

$$\begin{aligned}
H = & \sum_{\langle i,j\rangle} J_{zz}S^z_i S^z_j + J_{\pm}(S^+_i S^-_j + S^-_i S^+_j) \\
&+ J_{\pm\pm}(\gamma_{ij}S^+_i S^+_j + \gamma^*_{ij}S^-_i S^-_j) \\
&+ J_{\pm z}\left(\gamma^*_{ij}S^+_i S^z_j + \gamma_{ij}S^-_i S^z_j + \langle i \leftrightarrow j\rangle\right), \qquad \text{(A1)}
\end{aligned}$$

where $S^{\pm}_i = S^x_i \pm \mathrm{i}S^y_i$, and the phase factors γ_{ij} along the a_1, a_2, a_3 bonds (see Fig. 1(b)) are $\mathrm{e}^{\mathrm{i}2\pi/3}$, $\mathrm{e}^{-\mathrm{i}2\pi/3}$, 1 respectively.

There exists DM interaction in YOCl. Structurally, the nearest neighbor bonds have inversion symmetry according to their bond centers, but the next nearest-neighbor bond has no central inversion symmetry, so DM interactions are allowed. There is a mirror symmetry plane perpendicular to the next nearest-neighbor bond, so the DM vector is perpendicular to the bond.[70] Furthermore, the anion Cl^- is far away from the next-nearest bonds and have weaker effects, so the next nearest-neighbor rare-earth ions mainly exchange through the O^{2-} ions. And the DM vector $\boldsymbol{D}_{ij}$ is almost perpendicular to the triangular cation-layer plane. In the following discussion, we analyze the symmetry restraint to the direction of $\boldsymbol{D}_{ij}$, where (ij) is oriented in the counterclockwise manner.

Here we provide the orientation of the DM vector $\boldsymbol{D}_{ij}$ in the new spin coordinate system $\{x, y, z\}$ (see Fig. 1(c)). Firstly, we consider the component perpendicular to the honeycomb plane. In the new frame, $\boldsymbol{c} \parallel \frac{1}{\sqrt{3}}(1,1,1)$, so, $\boldsymbol{D} \parallel \frac{1}{\sqrt{3}}(1,1,1)$. Furthermore, owing to the D_{3d} symmetry, the c-components of the $\boldsymbol{D}_{ij}$ vector on the two sublattices have the same sign.

Then we analyze the in-plane components although they are relatively weak. Since the $\boldsymbol{D}$ vector is perpendicular to the next nearest-neighbor bond,[70] the allowed direction is one of $\pm\frac{1}{\sqrt{6}}(2x-y-z)$, $\pm\frac{1}{\sqrt{6}}(2y-z-x)$, $\pm\frac{1}{\sqrt{6}}(2z-x-y)$, depending on the bond direction.

References

[1] Ji J, Sun M, Cai Y, Wang Y, Sun Y, Ren W, Zhang Z, Jin F and Zhang Q 2021 *Chin. Phys. Lett.* **38** 047502
[2] AdyStern 2010 *Nature* **464** 187
[3] Shimizu Y, Miyagawa K, Kanoda K, Maesato M and Saito G 2003 *Phys. Rev. Lett.* **91** 107001
[4] Itou T, Oyamada A, Maegawa S and Kato R 2010 *Nat. Phys.* **6** 673
[5] Han T H, Helton J S, Chu S, Nocera D G, Rodriguez-Rivera J A, Broholm C and Lee Y S 2012 *Nature* **492** 406
[6] Depenbrock S, McCulloch I P and Schollwöck U 2012 *Phys. Rev. Lett.* **109** 067201
[7] Chen G and Balents L 2008 *Phys. Rev. B* **78** 094403
[8] Lawler M J, Kee H Y, Kim Y B and Vishwanath A 2008 *Phys. Rev. Lett.* **100** 227201
[9] Micklitz T and Norman M R 2010 *Phys. Rev. B* **81** 174417
[10] Kitaev A 2006 *Ann. Phys* **321** 2
[11] Chaloupka J c v, Jackeli G and Khaliullin G 2010 *Phys. Rev. Lett.* **105** 027204
[12] Nasu J, Knolle J, Kovrizhin D L, Motome Y and Moessner R 2016 *Nat. Rev. Phys.* **12** 912
[13] Barkeshli M, Berg E and Kivelson S 2014 *Science* **346** 722
[14] Shitade A, Katsura H, Kuneš J, Qi X L, Zhang S C and Nagaosa N 2009 *Phys. Rev. Lett.* **102** 256403
[15] Choi S K, Coldea R, Kolmogorov A N, Lancaster T, Mazin I I, Blundell S J, Radaelli P G, Singh Y, Gegenwart P, Choi K R, Cheong S W, Baker P J, Stock C and Taylor J 2012 *Phys. Rev. Lett.* **108** 127204
[16] Plumb K W, Clancy J P, Sandilands L J, Shankar V V, Hu Y F, Burch K S, Kee H Y and Kim Y J 2014 *Phys. Rev. B* **90** 041112
[17] Liu X, Berlijn T, Yin W G, Ku W, Tsvelik A, Kim Y J, Gretarsson H, Singh Y, Gegenwart P and Hill J P 2011 *Phys. Rev. B* **83** 220403
[18] Baek S H, Do S H, Choi K Y, Kwon Y S, Wolter A U B, Nishimoto S, van den Brink J and Büchner B 2017 *Phys. Rev. Lett.* **119** 037201
[19] Takayama T, Kato A, Dinnebier R, Nuss J, Kono H, Veiga L S I, Fabbris G, Haskel D and Takagi H 2015 *Phys. Rev. Lett.* **114** 077202

[20] Williams S C, Johnson R D, Freund F, Choi S, Jesche A, Kimchi I, Manni S, Bombardi A, Manuel P, Gegenwart P and Coldea R 2016 *Phys. Rev. B* **93** 195158

[21] Knolle J, Moessner R and Perkins N B 2019 *Phys. Rev. Lett.* **122** 047202

[22] Johnson R D, Williams S C, Haghighirad A A, Singleton J, Zapf V, Manuel P, Mazin I I, Li Y, Jeschke H O, Valentí R and Coldea R 2015 *Phys. Rev. B* **92** 235119

[23] Liu Z X and Normand B 2018 *Phys. Rev. Lett.* **120** 187201

[24] Zheng J, Ran K, Li T, Wang J, Wang P, Liu B, Liu Z X, Normand B, Wen J and Yu W 2017 *Phys. Rev. Lett.* **119** 227208

[25] Wolter A U B, Corredor L T, Janssen L, Nenkov K, Schönecker S, Do S H, Choi K Y, Albrecht R, Hunger J, Doert T, Vojta M and Büchner B 2017 *Phys. Rev. B* **96** 041405

[26] Yadav R, Bogdanov N A, Katukuri V M, Nishimoto S, van den Brink J and Hozoi L 2016 *Sci. Rep.* **6** 37925

[27] Banerjee A, Lampen-Kelley P, Knolle J, Balz C, Aczel A A,Winn B, Liu Y, Pajerowski D, Yan J, Bridges C A, Savici A T, Chakoumakos B C, Lumsden M D, Tennant D A, Moessner R, Mandrus D G and Nagler S E 2018 *npj Quantum Mater.* **3** 8

[28] Yao W and Li Y 2020 *Phys. Rev. B* **101** 085120

[29] Ran K, Wang J, Wang W, Dong Z Y, Ren X, Bao S, Li S, Ma Z, Gan Y, Zhang Y, Park J T, Deng G, Danilkin S, Yu S L, Li J X and Wen J 2017 *Phys. Rev. Lett.* **118** 107203

[30] Lin D, Ran K, Zheng H, Xu J, Gao L, Wen J, Yu S L, Li J X and Xi X 2020 *Phys. Rev. B* **101** 045419

[31] Rau J G, Lee E K H and Kee H Y 2014 *Phys. Rev. Lett.* **112** 077204

[32] Jackeli G and Khaliullin G 2009 *Phys. Rev. Lett.* **102** 017205

[33] Birol T and Haule K 2015 *Phys. Rev. Lett.* **114** 096403

[34] Banerjee A, Bridges C A, Yan J Q, Aczel A A, Li L, Stone M B, Granroth G E, Lumsden M D, Yiu Y, Knolle J, Bhattacharjee S, Kovrizhin D L, Moessner R, Tennant D A, Mandrus D G and Nagler S E 2016 *Nat. Mater.* **15** 733

[35] Wang W, Dong Z Y, Yu S L and Li J X 2017 *Phys. Rev. B* **96** 115103

[36] Laurell P and Okamoto S 2020 *npj Quantum Mater.* **5** 2

[37] Wang J, Normand B and Liu Z X 2019 *Phys. Rev. Lett.* **123** 197201

[38] Liu W, Zhang Z, Ji J, Liu Y, Li J, Wang X, Lei H, Chen G and Zhang Q 2018 *Chin. Phys. Lett.* **35** 117501

[39] Zhang Z, Li J, Liu W, Zhang Z, Ji J, Jin F, Chen R, Wang J, Wang X, Ma J and Zhang Q 2021 *Phys. Rev. B* **103** 184419

[40] Zhang Z, Ma X, Li J, Wang G, Adroja D T, Perring T P, Liu W, Jin F, Ji J, Wang Y, Kamiya Y, Wang X, Ma J and Zhang Q 2021 *Phys. Rev. B* **103** 035144

[41] Song K and Kauzlarich S M 1994 *Chem. Mater.* **6** 386

[42] Li Y, Chen G, Tong W, Pi L, Liu J, Yang Z, Wang X and Zhang Q 2015 *Phys. Rev. Lett.* **115** 167203

[43] Li Y, Liao H, Zhang Z, Li S, Jin F, Ling L, Zhang L, Zou Y, Pi L, Yang Z, Wang J, Wu Z and Zhang Q 2015 *Sci. Rep.* **5** 16419

[44] Li Y, Adroja D, Biswas P K, Baker P J, Zhang Q, Liu J, Tsirlin A A, Gegenwart P and Zhang Q 2016 *Phys. Rev. Lett.* **117** 097201

[45] Shen Y, Li Y D, Wo H, Li Y, Shen S, Pan B, Wang Q, Walker H C, Steffens P, Boehm M, Hao Y, Quintero-Castro D L, Harriger L W, Frontzek M D, Hao L, Meng S, Zhang Q, Chen G and Zhao J 2016 *Nature* **540** 559

[46] Xu Y, Zhang J, Li Y S, Yu Y J, Hong X C, Zhang Q M and Li S Y 2016 *Phys. Rev. Lett.* **117** 267202

[47] Li Y, Adroja D, Bewley R I, Voneshen D, Tsirlin A A, Gegenwart P and Zhang Q 2017 *Phys. Rev. Lett.* **118** 107202

[48] Luo Q, Hu S, Xi B, Zhao J and Wang X 2017 *Phys. Rev. B* **95** 165110

[49] Lu Y M and Ran Y 2011 *Phys. Rev. B* **84** 024420

[50] You Y Z, Kimchi I and Vishwanath A 2012 *Phys. Rev. B* **86** 085145

[51] Luo Z X and Chen G 2020 *SciPost Phys. Core* **3** 4

[52] Ross K A, Savary L, Gaulin B D and Balents L 2011 *Phys. Rev. X* **1** 021002

[53] Rau J G and Gingras M J P 2018 *Phys. Rev. B* **98** 054408

[54] Li Y D, Wang X and Chen G 2016 *Phys. Rev. B* **94** 035107

[55] Luo Q, Zhao J, Kee H Y and Wang X 2020 Preprint 1910.01562

[56] Luo Q, Hu S, Zhao J, Metavitsiadis A, Eggert S andWang X 2018 *Phys. Rev. B* **97** 214433

[57] Winter S M, Li Y, Jeschke H O and Valentí R 2016 *Phys. Rev. B* **93** 214431

[58] Suzuki T and Suga S I 2018 *Phys. Rev. B* **97** 134424

[59] Kanki K, Loison D and Schotte K D 2005 *Eur. Phys. J. B* **44** 309

[60] Gohlke M, Wachtel G, Yamaji Y, Pollmann F and Kim Y B 2018 *Phys. Rev. B* **97** 075126

[61] Janssen L, Andrade E C and Vojta M 2017 *Phys. Rev. B* **96** 064430

[62] Joshi D G 2018 *Phys. Rev. B* **98** 060405

[63] Gotfryd D, Rusnačko J, Wohlfeld K, Jackeli G, Chaloupka J C V and Oleś A M 2017 *Phys. Rev. B* **95** 024426

[64] Liu K, Sadoune N, Rao N, Greitemann J and Pollet L 2021 *Phys. Rev. Research* **3** 023016

[65] Rao N, Liu K, Machaczek M and Pollet L 2021 Preprint 2102.01103

[66] Wang S, Qi Z, Xi B, Wang W, Yu S L and Li J X 2021 *Phys. Rev. B* **103** 054410

[67] Park S, Nagaosa N and Yang B J 2020 *Nano Lett.* **20** 2741

[68] Gao Y H and Chen G 2020 *SciPost Phys. Core* **2** 4

[69] VillalbaME, Gómez Albarracín F A, Rosales H D and Cabra D C 2019 *Phys. Rev. B* **100** 245106

[70] Moriya T 1960 *Phys. Rev.* **120** 91